



# Radiation pattern of planar optoelectronic antennas for broadband continuous-wave terahertz emission

SIMON NELLEN,<sup>1,3</sup>  SEBASTIAN LAUCK,<sup>1</sup> GARRIT SCHWANKE,<sup>1</sup>  
MILAN DEUMER,<sup>1</sup> ROBERT B. KOHLHAAS,<sup>1</sup> LARS LIEBERMEISTER,<sup>1</sup>  
MARTIN SCHELL,<sup>1,2</sup> AND BJOERN GLOBISCH<sup>1,2,4</sup>

<sup>1</sup>Fraunhofer Institute for Telecommunications, Heinrich Hertz Institute, Einsteinufer 37, 10587 Berlin, Germany

<sup>2</sup>Technische Universität Berlin, Institut für Festkörperphysik, Hardenbergstraße 36, EW 5-1, 10623 Berlin, Germany

<sup>3</sup>simon.nellen@hhi.fraunhofer.de

<sup>4</sup>bjoern.globisch@hhi.fraunhofer.de

**Abstract:** In future wireless communication networks at terahertz frequencies, the directivity and the beam profile of the emitters are highly relevant since no additional beam forming optics can be placed in free-space between the emitter and receiver. We investigated the radiation pattern and the polarization of broadband continuous-wave (cw) terahertz emitters experimentally and by numerical simulations between 100 GHz and 500 GHz. The emitters are indium phosphide (InP) photodiodes with attached planar antenna, mounted on a hyper-hemispherical silicon lens and integrated into a fiber-pigtailed module. As both packaging and material of the emitter was identical for all devices, similarities and differences can be directly linked to the antenna structure. We found that the feeding point structure that connects photodiode and antenna has a large influence on the radiation pattern. By optimizing the feeding point, we could reduce side lobes from  $-2$  dB to  $-13$  dB and narrow the 6dB beam angle from  $\pm 14^\circ$  to  $\pm 9^\circ$  at 300 GHz.

© 2021 Optical Society of America under the terms of the [OSA Open Access Publishing Agreement](#)

## 1. Introduction

In the last decade, optoelectronic continuous-wave (cw) terahertz systems have evolved from purely spectroscopic tools in science labs to a promising technology for industrial applications [1,2]. In sensing, cw terahertz systems offer a bandwidth of more than 3.5 THz with measurement rates of a few tens of Hz [3]. This makes them ideal tools for the measurement of thin dielectric layers and imaging with in-depth resolution [4]. Compared to competing terahertz technologies like time domain spectroscopy (TDS) and purely electronic sources [5], optoelectronic cw systems are fully compatible with photonic and electronic integration technology [6,7], offer an enormous bandwidth [8] and do not rely on any moving parts [9] or optical phase-locking electronics [10,11]. In wireless communications, the increasing demand for high data rates and bandwidth has led to the development of communication links in the terahertz range based on photonics [12–15]. Frequency bands above 275 GHz have not yet been allocated to other active services. At such high carrier frequencies, extremely large bandwidths of over 50 GHz can be employed for radio communications [16]. Wireless communication links based on photonic components with a single channel data rate of more than 100 Gbit/s have been demonstrated only recently [14,17,18]. By choosing an optical excitation wavelength in the c-band (1530 nm to 1565 nm) mature and reliable components developed for fiber optical communications can be used to build compact and cost-efficient terahertz links directly compatible with the existing fiber optical infrastructure [13,14].

For all the aforementioned applications, the beam profile of the optoelectronic emitter is of great importance when terahertz optics cannot be used. In sensing, lens-less imaging requires knowledge about the frequency dependent radiation pattern of the emitter [19,20]. In wireless communication links, no additional beam forming optics between emitter and receiver can be employed, which also requires knowledge about the directivity and the beam profile of the emitter. However, a detailed study of the frequency dependent radiation pattern of quasi-optic, i.e. lens coupled, continuous-wave terahertz emitters is not available so far, which complicates the design both of sensor heads and communication links.

In this paper, we investigate the frequency dependent radiation pattern of lens coupled optoelectronic terahertz emitters employing waveguide integrated PIN photodiodes (PD) [21] and compare the results with frequency dependent simulations in ANSYS HFSS. These emitters are commercially available as broadband photomixers at TOPTICA Photonics AG. We find that the contact structure that connects the PIN PD with the bowtie antenna has a significant influence on the radiation pattern. By optimizing this feeding point, the radiation pattern of the emitters can be improved significantly.

## 2. Measurement of the radiation pattern

### 2.1. Bowtie emitter design

In this study we investigate the influence of three different feeding point geometries, which connect the waveguide integrated PIN PD with a bowtie antenna, on the radiation pattern of the emitter. Figure 1 shows the output power of these three bowtie (BT) antennas from 100 GHz to 500 GHz measured with a calibrated pyroelectric detector (THz20, Sensor- und Lasertechnik GmbH, Germany) [22]. Details of the measurement setup can be found in [23]. The three subplots in Fig. 1 illustrate the structure of the chip and antenna geometry for the three different feeding point designs. Note that the dimensions of the optical waveguide (WG) and the InP chip ( $1.5 \text{ mm} \times 3 \text{ mm}$ ) are identical in all three designs. The only difference is the antenna structure and the feeding point between photodiode (PD) and antenna. The augmented views below the power spectra show the different feeding point geometries. BT#1, which is a commercially available structure, is an extended bowtie, i.e. only the very tip of the antenna, which is connected to the feeding point of the PD, has a bowtie shape. The triangles are extended with  $400 \text{ }\mu\text{m}$  long rectangular patches, i.e. a dipole-shaped extension. The overall length of the antenna (top to bottom) is  $1 \text{ mm}$ . A straight metallic air-bridge connects the top p-contact of the PD mesa with the upper wing of the BT antenna. To reduce the series resistance of the PD, the n-contact is implemented as a bracket across the WG to both sides of the PD. This metallic bracket influences the frequency-dependent impedance of the whole antenna and results in the plateau of almost constant output power that can be observed between 250 GHz and 350 GHz in Fig. 1 [23]. Note that the electric field (E) is oriented parallel to the wings of the BT, i.e. the E-plane of BT#1 coincides with the short edge of the InP chip. BT#2 features the same extended BT geometry as BT#1. However, the connection between PD and BT antenna is essentially different: the PD is positioned in the center of the two wings of the BT and the connection from p- and n-contact are as short as possible. The intention of this design is to reduce the space between PD and antenna as much as possible at the expense of the impedance match. Note that this feeding point geometry does not result in any prominent spectral feature up to 500 GHz. BT#3 is essentially different from the last two designs. The antenna itself is designed in standard bowtie geometry of triangles and the PD is positioned between the left and right wing of the antenna. A short air-bridge connects the top p-contact of the diode mesa with the right wing of the antenna while the left wing is connected to the n-contact of the PD from both sides. This design tries to meet the original bowtie antenna as much as possible and minimizes the influence of the feeding point geometry. In order to realize this BT emitter, the antenna is rotated by  $90^\circ$  compared to the other two designs. Thus, the optical WG divides the left wing of the BT, with both halves connected

via metallic air-bridges across the WG. The overall length of the antenna (left to right) is 400  $\mu\text{m}$ . For this design, the E-plane of BT#3 is oriented along the long side of the antenna chip.

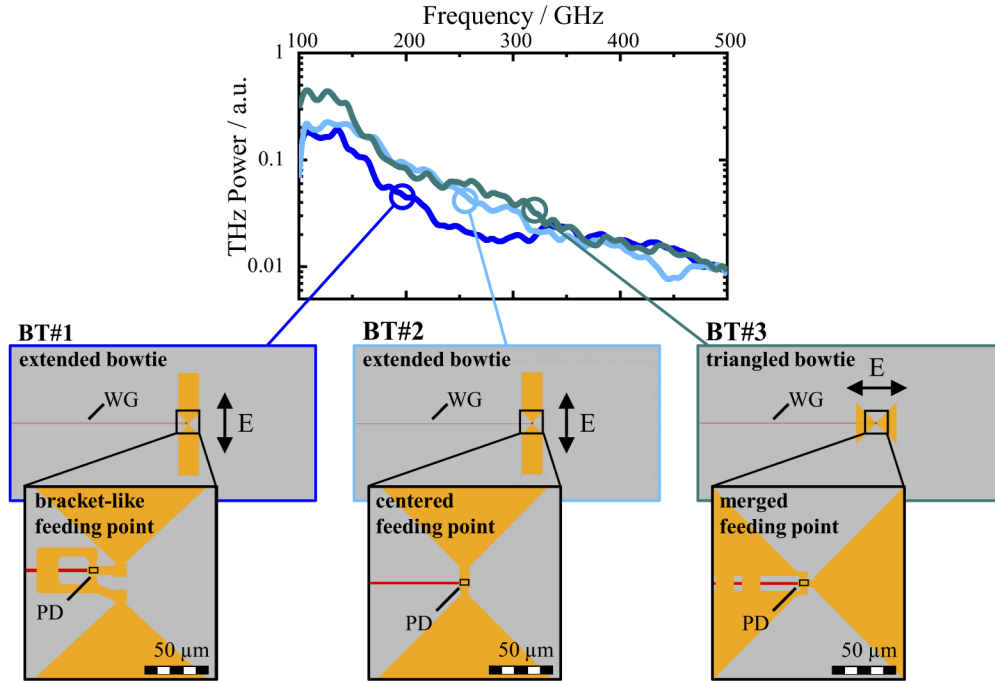


**Fig. 1.** Terahertz power as a function of frequency between 100 GHz and 500 GHz emitted by waveguide integrated PIN PDs with three different bowtie (BT) antenna structures. Insets show sketches of the different BT geometries: the optical waveguide WG (red line), the antenna structure (yellow) and the respective E-field orientation are displayed. The colored frame is the outline of the InP chip (1.5 mm  $\times$  3 mm). The augmented views illustrate the feeding points that connect PD and antenna.

## 2.2. Setup

A coherent cw terahertz spectrometer as shown in Fig. 2 is employed to measure the emitted terahertz field of the PIN PD emitters. Two C-band external cavity lasers (ECL) are used to create the optical beat note at the desired radiation frequency between 100 GHz and 500 GHz. A phase modulation unit (PMU) based on an electro-optical phase modulator allows for fast and coherent acquisition of the terahertz spectra [24]. Erbium doped fiber amplifiers (EDFA) amplify the optical beat signal to 30 mW in order to drive the different PIN-PD emitters (Tx) and the commercially available photoconducting receiver (Rx) [21]. Emitter and receiver are mounted on posts in direct line of sight without any additional optical elements. The electrical signal from the Rx is amplified with a transimpedance amplifier (TIA, Femto DLPCA-200) with  $10^6$  V/A gain. A lock-in amplifier (LIA) acquires amplitude and phase of the detector signal by synchronization with the modulation frequency ( $f_{\text{mod}} = 20$  kHz) of the PMU.

The distance between Tx and Rx measures 30 cm and the mounting height of the two modules is 20 cm. Consequently, the radiation angle for direct reflection of terahertz radiation at the metal bottom plate would be greater than  $50^\circ$ . Since no significant amount of radiation is measured at those angles, detrimental effects due to reflections can be neglected. Both emitter and receiver include a hyper-hemispherical silicon lens. Such a substrate-lens increases the directivity, reduces reflection losses at the interface between InP and air, and suppresses substrate-modes inside the

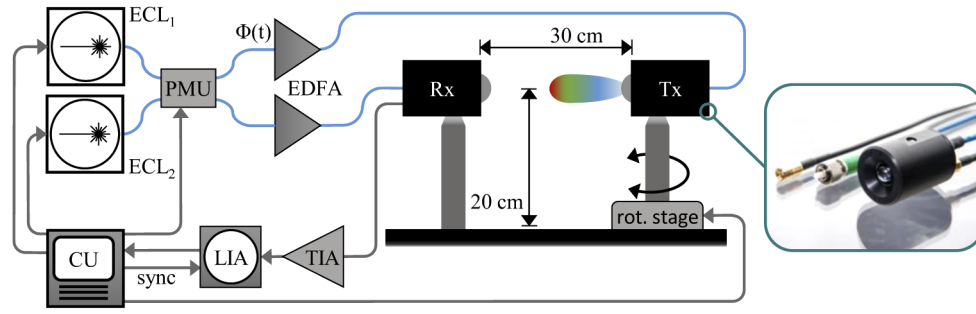


**Fig. 2.** Setup for the radiation pattern measurements: an electro-optical phase modulator unit (PMU) combines the signals of two external cavity lasers  $ECL_1$  and  $ECL_2$ . Erbium doped fiber amplifiers (EDFA) boost the power of the optical beat signals from the PMU to 30 mW before coupling into the emitter (Tx) and receiver (Rx), respectively. The optical beat signal of the emitter  $\Phi(t)$  is modulated. The rotation stage (rot. stage) allows rotation of Tx while the Rx is fixed at a distance of 30 cm. A transimpedance amplifier (TIA) pre-amplifies the detector signal before feeding it into a lock-in amplifier (LIA). The LIA synchronizes the detector signal with the modulation frequency (sync) to extract amplitude and phase of the terahertz signal. The control unit (CU) sets all measurement parameters and reads out the LIA. The photograph on the right depicts the fiber-pigtailed emitter module.

InP chip [25]. In combination with the large distance of 30 cm between emitter and receiver, the diameter of the silicon lens (10 mm) results in an acceptance angle of the setup of  $0.95^\circ$ .

The Fraunhofer criterion is widely accepted to define the beginning of the far-field region  $R_{ff}$

$$R_{ff} > 2 \frac{D^2}{\lambda}.$$

Hence, the diameter of the largest aperture of the emitter  $D$  and the wavelength  $\lambda$  determine the beginning of the far-field: the shorter the wavelength and the larger the aperture of the emitter are the larger is the near-field region. In order to ensure that our measurements were conducted in the far-field,  $\lambda$  and  $D$  have to be determined. For  $\lambda$ , we use the highest frequency generated in our experiments, which is 500 GHz. However, the determination of  $D$  is not straightforward for the experimental geometry investigated in this publication due to the following reason: the terahertz emitter consist of a bowtie antenna with a diameter  $\leq 1$  mm on top of an InP substrate, which is attached to a silicon lens with a diameter of 10 mm. Hence, the question arises whether the diameter of the antenna, the diameter of the substrate lens or something in between defines the largest aperture of the emitter. In the first case, one may assume that the InP chip radiates into a half-space of silicon and the actual radiator is the bowtie antenna  $D_{BT} \leq 1$  mm. With the refractive index of the silicon lens ( $n_{Si} = 3.4$ ) the far-field region of the emitter begins approx. 11.3 mm behind the emitter at 500 GHz. However, the total thickness of substrate and silicon lens measures 6.45 mm only. Thus, the near-field region extends approx. 2.6 mm into the free-space behind the Si lens at 500 GHz [26]. Under this assumption, the distance of 30 cm between emitter and detector employed in our experiments is sufficient to ensure far-field measurements. However, in microwave literature the dielectric lens is often referred as part of the antenna [27–29]. In that case, the surface of the lens acts as the radiator and the largest aperture of our emitters is determined by the illuminated area of the silicon lens. Under this assumption, the distance of 30 cm between emitter and receiver would be sufficient for far-field measurements at 500 GHz if the effective aperture was smaller than  $D_{eff} \leq 9.5$  mm. This criterion is clearly fulfilled for our emitters. Hence, we assume that we measure the far-field radiation pattern of our emitters by using the experimental setup shown in Fig. 2.

For the measurement of the radiation pattern, the receiver is fixed and points toward the emitter, which is mounted on a rotation stage. The emitter rotates between  $-90^\circ$  and  $+90^\circ$  in steps of  $0.5^\circ$ , where  $0^\circ$  corresponds to a straight alignment toward the receiver. The control unit (CU) captures a coherent terahertz spectrum between 100 GHz and 500 GHz with a sub-GHz frequency resolution for each position of the emitter. In order to ensure undistorted results the rotation axis coincides with the virtual focal point of the divergent emitter, which is located  $22 \text{ mm} \pm 1 \text{ mm}$  behind the front side of the emitter. The radiation pattern of E- and H-plane are measured by orienting Tx and Rx with the respective polarization: for the E-plane, the orientation of the electric field E of emitter and receiver antenna are perpendicular to the rotation axis and for the H-plane, the magnetic field H is perpendicular to the rotation axis.

### 2.3. Comparison of three types of bowtie

In this subsection the frequency dependent radiation pattern of the three antenna structures BT#1, BT#2 and BT#3 (c.f. Fig. 1) is investigated. The upper three heat maps of Fig. 3 show the E-plane radiation pattern of BT#1, BT#2 and BT#3 in units of intensity, i.e.  $E^2$ . Here, red color corresponds to high intensity while blue color indicates lower intensities down to  $-30 \text{ dB}$  below the maximum value. The maximum intensity measured for each frequency point is set to  $0 \text{ dB}$ , i.e. intensities are normalized to the respective intensity maximum for each frequency point. This normalization allows the analysis of the radiation pattern for this broad frequency range of more than 400 GHz in a single plot. The black contour line, which can be seen in each subplot, indicates a decrease of the intensity to  $-3 \text{ dB}$  from its maximum. For BT#1 the 3dB-range is centered at  $0^\circ$  up to 350 GHz with decreasing width for higher frequencies. However, beyond 350 GHz the main lobe of BT#1 tilts towards  $+10^\circ$  and the 3dB-width does not further decrease. Additionally, side lobes appear. Note that the intensity of these side lobes is lower than  $-3 \text{ dB}$  except for a few isolated spots. For frequencies below 350 GHz, the side lobes approach the main lobe with increasing frequency. Beyond 350 GHz the angular position of side lobes does not change significantly.

We compare BT#1 and BT#2 in order to investigate the influence of the feeding point geometry, which connects the PIN-PD with the bowtie antenna, on the radiation pattern of the emitter. Up to 250 GHz the shape of the main lobe of both designs is almost identical. For BT#2, strong side lobes appear at  $\pm 20^\circ$  for frequencies above 125 GHz, which approach the main lobe for higher frequencies. Beyond 250 GHz the main lobe merges with these side lobes. Compared to BT#1 the side lobes have an overall higher intensity. At frequencies  $> 250 \text{ GHz}$ , the width of the main lobe of BT#2 is approx.  $\pm 10^\circ$ . However, the main lobe of BT#2 does not shift from its central position, as is the case for BT #1. In contrast to BT#1, new side lobes arise at angular positions between  $\pm 20^\circ$  and  $\pm 30^\circ$ .

From this comparison, we attribute the asymmetric radiation pattern of BT#1 to its asymmetric feeding point structure. The tilt of the main lobe of BT#1 for frequencies  $> 300 \text{ GHz}$  implies that the asymmetric feeding point structure becomes a radiative element at these frequencies, as it is no more electrically small compared to the wavelength. Indeed, the bracket-like structure of BT#1 measures about a quarter wavelength at 350 GHz. In addition, the extended bowtie seems to be the reason for the high number of side lobes. The rectangular extension appears to act as a broad dipole, which leads to the generation of side lobes that have different angular positions for different frequencies.

Up to 425 GHz, the H-plane of BT#1 and BT#2 features a centered main lobe with decreasing 3dB-width at higher frequencies. Beyond 425 GHz, the H-plane consists of two symmetric lobes. Although these lobes arise at slightly different frequencies for BT#1 and BT#2, we assign this feature to the dimension of the InP substrate and not to the antenna structure. We discuss this in more detail in the comparison to BT#3.



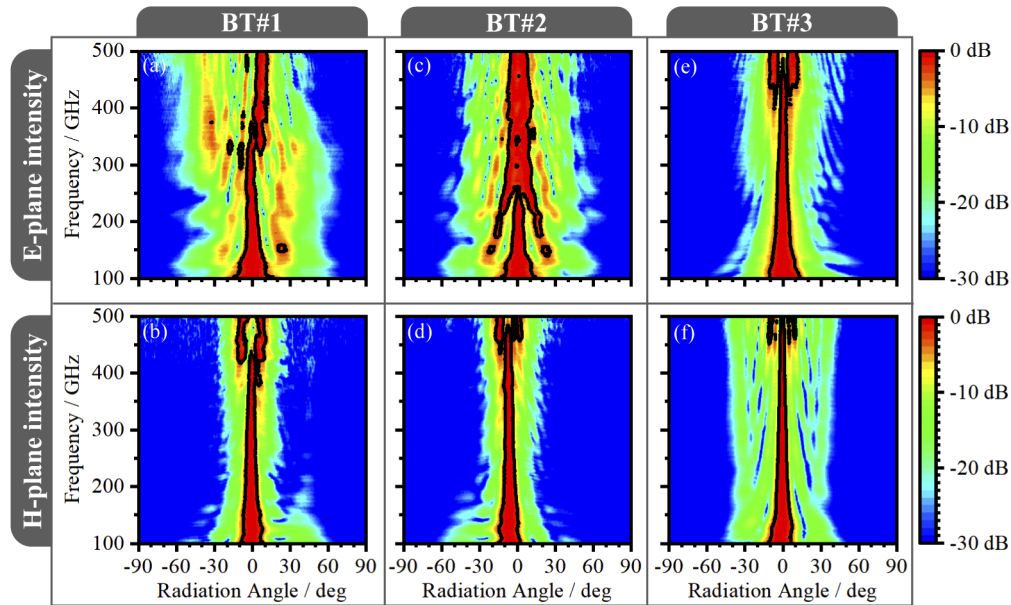


**Fig. 3.** Radiation pattern of the three different types of bowties measured from 100 GHz to 500 GHz for angles between  $-90^\circ$  and  $90^\circ$ : (a) E-plane and (b) H-plane of BT#1. (c) E-plane and (d) H-plane of BT#2. (e) E-plane and (f) H-plane of BT#3. The intensity is normalized to the maximum at each frequency. The black contour line indicates the 3 dB beam angle.

The E-plane of BT#3 [Fig. 3(e)] shows a centered main lobe up to 425 GHz. The 3dB-width is  $\pm 10^\circ$  at 100 GHz and decreases for higher frequencies. The very clean radiation pattern is a result of the pure bowtie shape of the antenna and the short connection between bowtie and photodiode, i.e. the diode merges with the feeding point of the antenna. Around 400 GHz the 3dB-width is less than  $\pm 5^\circ$ . Beyond 450 GHz, the E-plane of BT#3 consists of two additional lobes located at  $\pm 10^\circ$ . This pattern is very similar to the H-plane of BT#1 and BT#2 in Figs. 3(b) and 3(d), respectively. While feeding point and antenna structure of BT#1 and BT#2 are essentially different from BT#3, the dimension of the InP is the same for all three structures. The only difference is the orientation of the diode and the antenna on the chip. As depicted in Fig. 1 the orientation of the E-field of BT#3 is rotated by  $90^\circ$  compared to the two other designs. Thus, the dimension of the InP substrate is the common property of the H-plane of BT#1 and BT#2 and the E-plane of BT#3, respectively. Consequently, we assign the side lobes in the H-plane of BT#1 and BT#2 and the E-plane of BT#3 to the chip boundaries, i.e. to reflections at the interface between InP substrate and air [25,30].

In the H-plane of BT#3 [Fig. 3(f)] side lobes are suppressed to less than  $-10$  dB compared to the intensity of the narrow main lobe up to 450 GHz. However, side lobe exist for frequencies beyond 450 GHz even though they are less prominent than for BT#1 and BT#2.

In order to evaluate the reproducibility of the radiation pattern in terms of antenna fabrication, packaging and measurement we characterized three individual emitter modules of BT#1. Figure 4 illustrates the average intensity of the E-plane (a) and H-plane (b). The comparison between a single BT#1 [Figs. 3(a) and 3(b)] and the average of three emitters shows a high reproducibility of the packaging and measurement process. Figures 4(c) and 4(d) show the standard deviation of the three BT#1 emitters. The black lines in those plots indicate the  $-3$  dB contour of the averaged E- and H-plane. Note that the standard deviation is close to zero (dark blue) within the 3dB-range

of the radiation pattern. Deviations of more than 3 dB (green areas) appear only for those angular positions where the intensity is at least  $-10$  dB below the intensity of the main lobe. Thus, we conclude that all features observed in the radiation patterns stem from the chip itself whereas the influence of packaging-related tolerances and measurement uncertainties is negligible.

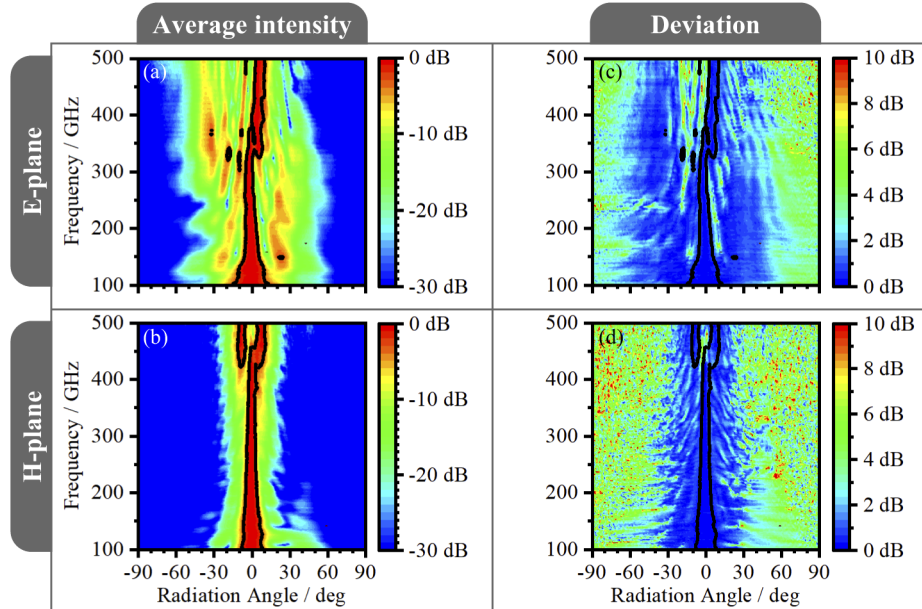


**Fig. 4.** Analysis of deviation between radiation patterns of three individual emitters with BT#1: (a) average E-plane and (b) average H-plane normalized to the maximum of each frequency from 100 GHz to 500 GHz for angles between  $-90^\circ$  and  $90^\circ$ . The standard deviation of (c) E-field and (d) H-field due to averaging is a measure for the reproducibility of the radiation pattern. The black line in (c) and (d) indicates the 3 dB beam angle from (a) and (b), respectively. Note there is 0 dB deviation within the 3 dB range for nearly all frequencies.

### 3. Numerical simulation of radiation pattern

For the design and development of RF components, numerical simulations are essential. In this section, we compare the experimental data presented in the previous section with numerical simulations. We simulated the radiation pattern with Ansys HFSS. The model includes the full antenna structure, the InP substrate and the silicon lens. The metallic housing was not part of the 3D-model as the dimensions compared to the wavelength are too big for reasonable computing effort. In addition, we verified experimentally that the influence of the housing is negligible.

Figure 5 compares simulated (red) and measured (black) radiation patterns of BT#1 for 100 GHz, 200 GHz and 300 GHz (left to right) and angles between  $+90^\circ$  and  $-90^\circ$ . For the simulations at 100 GHz we employed the finite element method (FEM) with an adaptive mesh. Due to the increased computing effort, the adaptive mesh could not be used for frequencies higher than 150 GHz. Thus, FEM simulations at 200 GHz employed the mesh calculated for 150 GHz. In order to avoid under-meshing we used a hybrid simulation method employing FEM and method of moments (MoM) at 300 GHz. Although the hybrid method drastically increased the simulation time, an adaptive mesh could be used.

Overall, position and shape of the main lobe for both, E-plane (upper sub-plot) and H-plane (lower sub-plot) agree very well between simulation and measurement. Moreover, the position of

BT#1: Simulation (—) and Measurement (—)

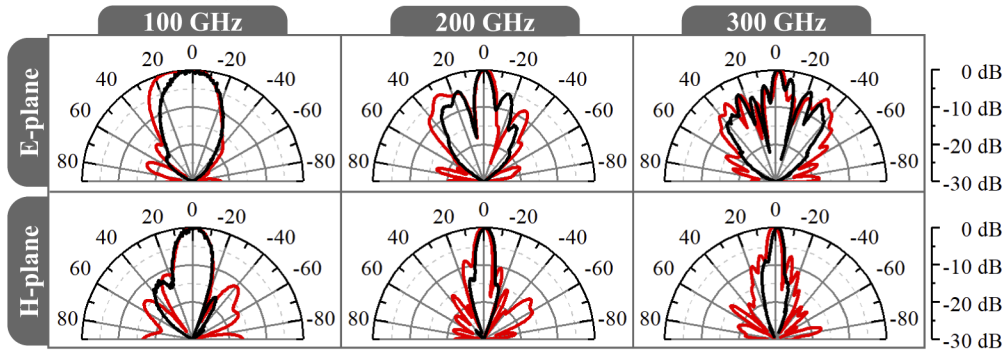


**Fig. 5.** Simulated (red) and measured (black) radiation pattern of BT#1 from  $-90^\circ$  to  $90^\circ$  at 100 GHz, 200 GHz and 300 GHz (from left to right). Upper (lower) plots show the intensity of the E-plane (H-plane).

the measured side lobes is in good agreement with the simulations up to an angle of  $\pm 60^\circ$  and  $\pm 20^\circ$  for the E-plane and H-plane, respectively. While the simulated E-plane at 100 GHz shows a very broad main lobe, the measured main lobe is narrower and symmetric. Additionally, the measurement reveals only one side lobe at  $50^\circ$  in good agreement with the simulation. Since the peak intensity of the side lobe is  $-20$  dB, the deviation of 4 dB between measurement and simulation is negligible. For the H-plane at 100 GHz, the measured main lobe matches perfectly with the simulation. However, a side lobe predicted at  $+25^\circ$  appears at approx.  $+30^\circ$ . At 200 GHz position and width of the main lobe match for E- and H-plane. While the position of the measured side lobes agree with the simulation, the intensity is lower than predicted. In the E-plane at 200 GHz, prominent side lobes appear at  $\pm 18^\circ$  with approx.  $-5$  dB intensity, which differs from the asymmetric radiation pattern calculated by the simulation. At 300 GHz, the measured radiation pattern in the H-plane is more directional than predicted by our simulation. Moreover, the simulation shows a high number of fringes, which are not found in the experimental data. In contrast, the measured E-plane at 300 GHz widely confirms the predictions of the simulation: A high number of side lobes exist up to  $\pm 40^\circ$ , while the intensity of all side lobes is more than 3 dB lower than the intensity of the main lobe. However, we find a good agreement between measurement and simulation, which indicates that the 3D-model of the diode, the feeding point and the antenna represents the essential components influencing the radiation pattern.

The comparison between measurement and simulation for BT#3 is shown in Fig. 6. The simulation was conducted with the same methods and boundary conditions as for BT#1. The color-coding and the arrangement of the subplots is also identical to Fig. 5. In general, simulation and measurement of BT#3 agree very well except from side lobes that appear at levels of  $-20$  dB below the peak intensity of the main lobe. In addition, all measured radiation patterns feature a lower number of side lobes with lower intensity than the corresponding simulation. In comparison to BT#1, the radiation pattern of BT#3 shows a smaller number of side lobes with lower intensity. This is an enormous improvement of the radiation pattern caused by the improved feeding point and bowtie design of BT#3. In addition, the simulation confirms that no side lobes appear in E- (upper sub-plot) and H-plane (lower sub-plot) of BT#3 with an intensity higher than 10 dB at 100 GHz and 200 GHz. At 100 GHz, the width of the main lobe in E- and H-plane of BT#3 is very similar to BT#1. In contrast, the prominent side lobes and fringes that arise for BT#1 at 200 GHz do not appear for BT#3. Instead, the E-plane of BT#3 consist of a single main lobe with a  $-3$  dB width of less than  $\pm 5.5^\circ$ . For the H-plane at 200 GHz, the width of the main lobe is even narrower than in the E-plane for both measurement and simulation. Side lobes appear



with an amplitude lower than  $-12$  dB. At 300 GHz, however, the hybrid simulation of FEM and MoM predict a broadened main lobe of the E-plane compared to 200 GHz. Moreover, the shape of the simulated main lobe suggests a superposition of several lobes. The measured E-plane at 300 GHz does not confirm this. Instead, the  $-3$  dB width of the main lobe is smaller than  $\pm 3.5^\circ$ . As for all frequencies, the H-plane at 300 GHz provides an even lower  $-3$  dB width of the main lobe. Although the simulation predicts side lobes of  $-8$  dB at  $\pm 10^\circ$ , the measured intensity is less than  $-10$  dB.

**BT#3: Simulation (—) and Measurement (—)**

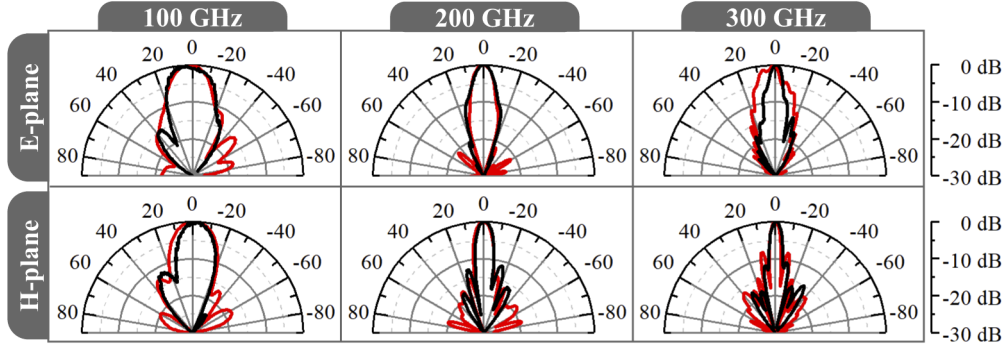


**Fig. 6.** Simulated (red) and measured (black) radiation pattern of BT#3 from  $-90^\circ$  to  $90^\circ$  at 100, 200 and 300 GHz (from left to right). The upper plots show the intensity of the E-plane, while the lower plots correspond to the H-plane.

The absence of side lobes for angular displacements higher than  $60^\circ$  is due to the rotation around the virtual focus point. For these angles, emitter and receiver are no longer in line of sight. In order to make sure that the metallic housing of the emitters did not influence the radiation pattern for larger rotation angles, we removed the critical parts of the housing next to the silicon lens and repeated the measurements. We did not find any significant change of the measured intensities for measurements with and without housing.

#### 4. Polarization

In this section, we investigate the polarization of the emitted terahertz radiation in detail. The antennas are designed for emitting linearly polarized terahertz radiation. By employing a wire grid polarizer between emitter and receiver in our setup, we measured the fraction of the radiation that was emitted in the unintended polarization. In addition, we investigated the different feeding point designs (see Fig. 1) for their ability to improve the linear polarization of the emitter.

In a first experiment, we added a wire grid polarizer in the setup for absolute power measurements with the pyroelectric thin film detector as described in section 2.1. Figures 7(a) and 7(c) show the frequency dependent output power for two orthogonal orientations of the polarizer between 100 GHz and 500 GHz for BT#1 and BT#3, respectively. A power spectrum without polarizer (solid line) serves as reference. When the polarizer is aligned with the main polarization axis of the emitter (E-plane), the terahertz power spectrum is almost unaffected by the polarizer for BT#1 and BT#3 (dotted line). If the polarizer is rotated by  $90^\circ$  an attenuation of about 10 dB is measured. For BT#1 [Fig. 7(a)], one can observe that the detected terahertz power is less than 10 dB above the noise level of the detector for frequencies higher than 300 GHz. Thus, the attenuation of the polarizer appears to be less than 10 dB for those frequencies.

In order to investigate the polarization of the radiated terahertz power in more detail, we rotated the polarizer between  $-90^\circ$  and  $+90^\circ$  with respect to the main polarization axis of the emitter (E-plane) and plotted the results in Figs. 7(b) (BT#1) and 7(d) (BT#3). The dashed gray line

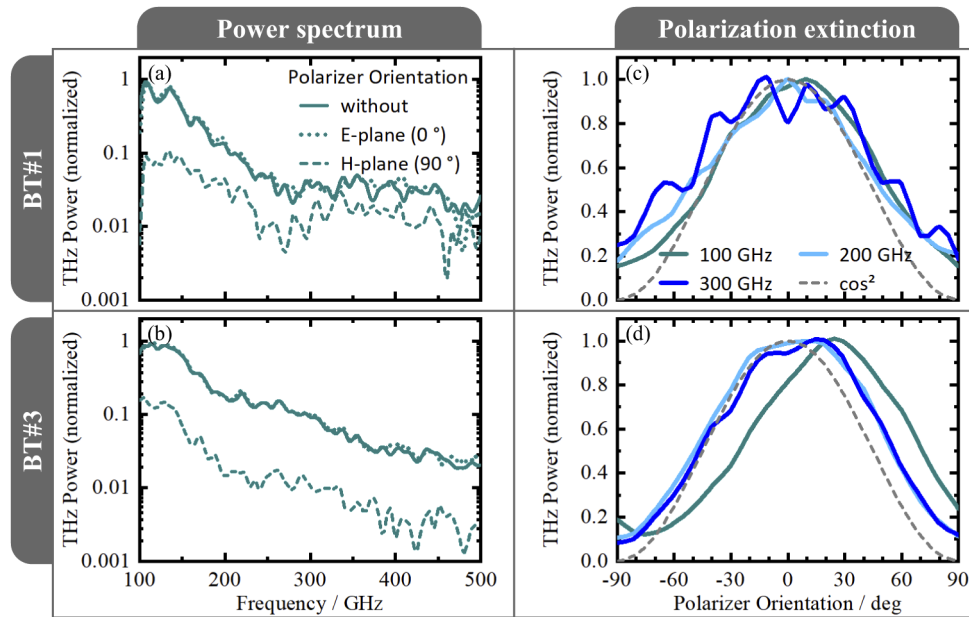
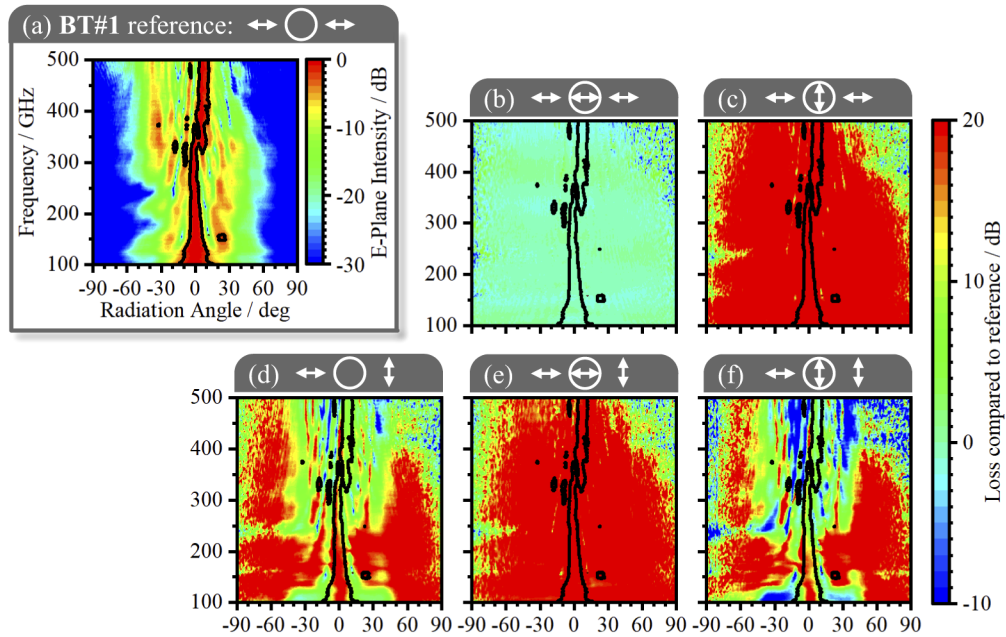


**Fig. 7.** Measured terahertz power between 100 GHz and 500 GHz for BT#1 (a) and BT#3 (c): without polarizer (solid line), with polarizer between emitter and receiver aligned to the E- plane (dotted line) and to the H-plane (dashed line). Emitter power of BT#1 (b) and BT#3 (d) at 100 GHz, 200 GHz and 300 GHz for polarizer orientations between  $-90^\circ$  and  $+90^\circ$ . The polarization extinction of a linearly polarized radiator is shown as a dashed gray line ( $\cos^2$ ).

indicates the ideal polarization extinction of a linearly polarized radiator, which corresponds to a  $\cos^2$  function. For 100 GHz, the maximum is shifted to  $10^\circ$  (BT#1) and  $20^\circ$  (BT#3). However, at 200 GHz the maximum matches the assumed  $0^\circ$  polarization for both antennas. Note that the low dynamic range of the 300 GHz pattern of BT#1 stems from noisy data caused by the low terahertz output power. The measured extinction ratio reveals a full width at half maximum (FWHM) of about  $100^\circ$  for BT#1 and BT#3, which is  $10^\circ$  higher than expected for a perfect linear polarized emitter. In conclusion, both emitters are not perfectly linearly polarized.

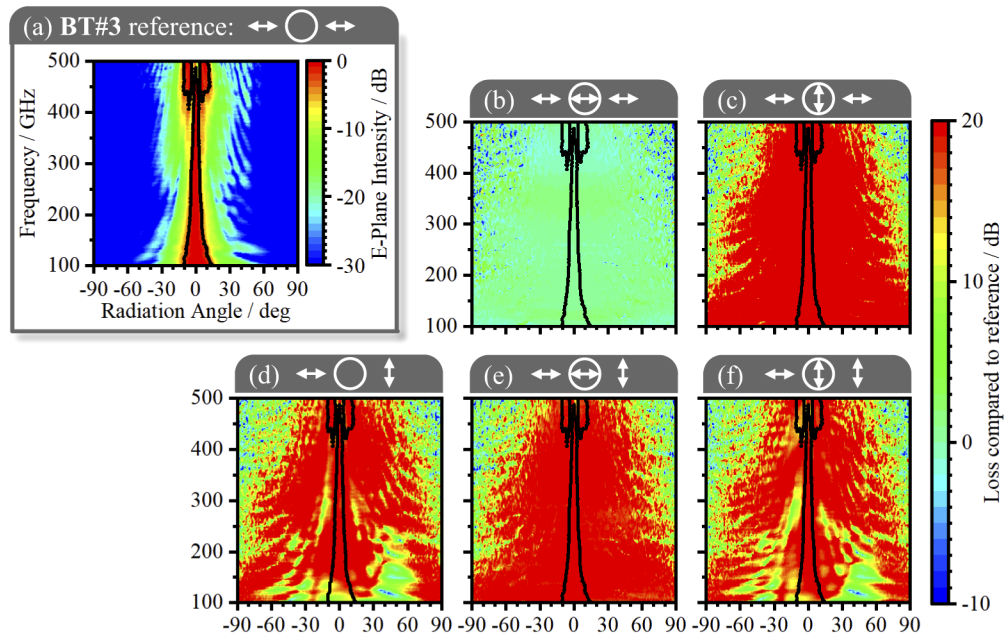
In order to investigate the emission of BT#1 and BT#3 in the E- and H-plane in more detail we measured radiation patterns with the coherent receiver in analogy to Fig. 3 and Fig. 4 for different orientations of the polarizer. Note that the coherent, photomixing receiver is designed for receiving linearly polarized terahertz radiation, which is underlined by the results presented in the next paragraph. In order to reduce the number of plots, we restrict our analysis to the radiation patterns of the E plane of the two emitters (see Figs. 8 and 9). Arrows indicate the orientation of the E-plane of the emitter, the transmission axis of the polarizer and the polarization of the receiver (from left to right). Figures 8(a) and 9(a) serve as a reference for subplots (b) – (f) as they depict the radiation pattern without polarizer (empty circle) and parallel orientation of emitter and receiver. Thus, Figs. 8(a) and 9(a) are identical to Figs. 3(a) and 4(a). The color-coding of all other subplots (b) – (f) is given in dB loss with respect to subplot (a). Red color indicates high loss whereas green to blue color indicates low loss.

Figure 8 shows the E-plane radiation pattern of BT#1 for different orientations of the polarizer and the coherent receiver. In Fig. 8(b) the E-plane of the emitter, the transmission axis of the polarizer and the polarization axis of the receiver are aligned. Thus, the polarizer attenuates the radiation emitted in the H-plane. As can be seen, the loss is small for all frequencies, i.e. the



**Fig. 8.** E-plane radiation pattern of BT#1 for different orientations of the polarizer and the receiver antenna for frequencies between 100 GHz and 500 GHz and rotation angles between  $-90^\circ$  and  $+90^\circ$ . Symbols in the upper right corner of each subplot indicate the orientation of the emitter, the polarizer and the receiver antenna, respectively. An empty circle indicates that no polarizer is inserted in the setup whereas an arrow in the circle indicates the transmission axis of the polarizer. Arrows left and right of the circle indicate the E-plane of emitter and the receiver, respectively. The radiation pattern in (a) is given in units of normalized intensity and serves as a reference for the subplots (b) – (f), which are color coded as loss in dB compared to (a). Red color indicates high loss whereas green to blue color indicates low loss. The black lines in each subplot are the  $-3$  dB contour of (a). Note that (d) – (f) indicate a polarization crosstalk of the emitter within the 3 dB range for 250 GHz to 500 GHz (green to blue).

main part of the radiation is emitted in the E-plane as expected from the design. In Fig. 8(c) the polarizer is rotated by  $90^\circ$  with respect to Fig. 8(b) whereas emitter and receiver remain aligned in the E-plane. In this configuration, the polarizer attenuates the radiation emitted in the E-plane. The high loss (red color) for all frequencies and radiation angles indicates again that most of the power is radiated in the E-plane. In Figs. 8(d) – 8(f) the orientation of emitter and receiver is orthogonal to each other, whereas no polarizer (8d), a polarizer oriented in parallel to the E-plane of the emitter (8e) and a polarizer oriented perpendicular to the E-plane of the emitter (8f) is inserted. By comparing the three plots one observes that Figs. 8(d) and 8(f) are very similar whereas Fig. 8(e) is almost identical to Fig. 8(c). This can be understood as follows: In Fig. 8(d), the receiver detects the radiation that is emitted in the H-plane. The green color in this plot indicates that this unintended emission is quite high outside the  $-3$  dB areas highlighted by the solid black lines. Thus, a considerable fraction of the radiation emitted by BT#1 ( $-4$  dB to  $-10$  dB with respect to the maximum of each frequency) is emitted into the wrong polarization axis. However, from this plot it is not yet clear how much of this radiation stems from emission in the wrong axis and how much is due to the receiver, which may not be entirely linearly polarized. This influence of the receiver is ruled out by subplots (e) and (f). In Fig. 8(e), the polarizer attenuates the radiation that is emitted by BT#1 in the H-plane. In this case, the overall loss is



**Fig. 9.** E-plane radiation pattern of BT#3 for different orientations of the polarizer and the receiver antenna for frequencies between 100 GHz and 500 GHz and rotation angles between  $-90^\circ$  and  $+90^\circ$ . Color-coding and plot arrangement are identical to Fig. 8.

extremely high. Consequently, the receiver does not detect E-plane radiation that is emitted in the H-plane of the receiver, which underlines the linear polarization of the receiver. In contrast, the configuration of Fig. 8(f) shows that the radiation, which is detected in the receiver's E-plane, is actually emitted by BT#1 as the polarizer in (f) attenuates the E-plane radiation of the emitter. Thus, we conclude that a measurable fraction of the radiation emitted by BT#1 has an unintended polarization. Again, we attribute this to the feeding point structure of this antenna. The bracket like contact design of BT#1 (see Fig. 1) leads to the emission into the unintended polarization.

This interpretation is underlined by the radiation pattern of BT#3 shown in Fig. 9. Please note that the arrangement and the color-coding of the subplots in Fig. 9 is identical to Fig. (8). Therefore, we can directly compare the corresponding subplots. In the following, we will restrict our analysis to the main differences between Figs. 8 and 9. The most important difference can be observed in Figs. 9(d) and 9(f). Compared to the same subplots in Fig. 8 one observes more red color, which indicates higher loss. Thus, BT#3 emits much less radiation in the unintended polarization. For frequencies below 200 GHz, BT#3 emits radiation into the H-plane for radiation angles higher than  $30^\circ$ . Note that the intensity at these angles is already  $-15$  dB compared to the main lobe. For higher frequencies, the radiation is almost linearly polarized for all radiation angles. We attribute this also to the feeding point design of BT#3 (see Fig. 1). Consequently, this design not only improved the radiation pattern but also suppressed terahertz emission into the wrong polarization axis.

## 5. Conclusion

In this paper, we investigated the radiation pattern and the polarization of three different broadband continuous-wave (cw) terahertz emitters between 100 GHz and 500 GHz. The emitters contained an indium phosphide (InP) based photodiode (PD) with planar bowtie antenna, which was mounted on a hyper-hemispherical silicon lens and integrated into a fiber-pigtailed module. The



main difference between the three emitters was the design of the feeding point, which is the electrical connection between PD and antenna, and the shape of the bowtie. We observed that the feeding point design has an enormous impact on both the radiation pattern and the polarization of the emitted terahertz radiation: i) feeding point structures with a dimension close to the wavelength of the emitted terahertz signal radiate and, thus, distort the main lobe. ii) Symmetric feeding points and structures along the E-plane of the antenna increase the polarization extinction ratio. In addition, we verified our experimental results with high frequency simulations. In order to suppress side lobes and obtain linear polarized terahertz emission in the E-plane of the emitter, the antenna design should resemble the original bowtie as much as possible and minimize the influence of the feeding point geometry. In our optimized design, the PD is positioned between upper and lower wing of the antenna and a short air bridge connects the top p-contact of the diode mesa with the upper wing of the antenna while the lower wing is connected to the n-contact of the PD from both sides. For example, this design suppresses unwanted side lobes at 300 GHz by more than 10 dB, narrows the main lobe from  $\pm 14^\circ$  to  $\pm 9^\circ$  and leads to almost linear polarization of the emitter. As the improvement of the radiation pattern of broadband terahertz emitters is especially important for applications in lensless imaging and wireless communication, this work is an important step towards improving the signal quality of optoelectronic cw terahertz systems for these applications.

**Funding.** Bundesministerium für Bildung und Forschung (16KIS0638); H2020 Industrial Leadership (871668).

**Disclosures.** The authors declare no conflicts of interest.

## References

1. S. Preu, G. H. Döhler, S. Malzer, L. J. Wang, and A. C. Gossard, "Tunable, continuous-wave terahertz photomixer sources and applications," *J. Appl. Phys.* **109**(6), 061301 (2011).
2. M. Naftaly, N. Vieweg, and A. Deninger, "Industrial applications of terahertz sensing: State of play," *Sensors* **19**(19), 4203 (2019).
3. L. Liebermeister, S. Nellen, R. Kohlhaas, S. Breuer, M. Schell, and B. Globisch, "Ultra-fast, high-bandwidth coherent cw THz spectrometer for non-destructive testing," *J. Infrared, Millimeter, Terahertz Waves* **40**(3), 288–296 (2019).
4. D. M. Mittleman, "Twenty years of terahertz imaging [invited]," *Opt. Express* **26**(8), 9417–9431 (2018).
5. N. S. Schreiner, W. Sauer-Greff, R. Urbansky, G. von Freymann, and F. Friederich, "Multilayer thickness measurements below the rayleigh limit using fmcw millimeter and terahertz waves," *Sensors* **19**(18), 3910 (2019).
6. M. Theurer, T. Göbel, D. Stanze, U. Troppenz, F. Soares, N. Grote, and M. Schell, "Photonic-integrated circuit for continuous-wave THz generation," *Opt. Lett.* **38**(19), 3724 (2013).
7. M. Smit, X. Leijtens, H. Ambrosius, E. Bente, J. Van Der Tol, B. Smalbrugge, T. De Vries, E. J. Geluk, J. Bolk, R. Van Veldhoven, L. Augustin, P. Thijs, D. D'Agostino, H. Rabbani, K. Lawniczuk, S. Stopinski, S. Tahvili, A. Corradi, E. Kleijn, D. Dzubrou, M. Felicetti, E. Bitincka, V. Moskalenko, J. Zhao, R. Santos, G. Gilardi, W. Yao, K. Williams, P. Stabile, P. Kuindersma, J. Pello, S. Bhat, Y. Jiao, D. Heiss, G. Roelkens, M. Wale, P. Firth, F. Soares, N. Grote, M. Schell, H. Debregeas, M. Achouche, J. L. Gentner, A. Bakker, T. Korthorst, D. Gallagher, A. Dabbs, A. Melloni, F. Morichetti, D. Melati, A. Wonfor, R. Pentty, R. Broeke, B. Musk, and D. Robbins, "An introduction to InP-based generic integration technology," *Semicond. Sci. Technol.* **29**(8), 083001 (2014).
8. A. D. J. F. Olvera, H. Lu, A. C. Gossard, and S. Preu, "Continuous-wave 1550 nm operated terahertz system using ErAs:In(Al)GaAs photo-conductors with 52 dB dynamic range at 1 THz," *Opt. Express* **25**(23), 29492 (2017).
9. N. Vieweg, F. Rettich, A. Deninger, H. Roehle, R. Dietz, T. Göbel, and M. Schell, "Terahertz-time domain spectrometer with 90 dB peak dynamic range," *J. Infrared, Millimeter, Terahertz Waves* **35**(10), 823–832 (2014).
10. M. Yahyapour, A. Jahn, K. Dutzi, T. Puppe, P. Leisching, B. Schmauss, N. Vieweg, and A. Deninger, "Fastest thickness measurements with a terahertz time-domain system based on electronically controlled optical sampling," *Appl. Sci.* **9**(7), 1283 (2019).
11. A. Bartels, R. Cerna, C. Kistner, A. Thoma, F. Hudert, C. Janke, and T. Dekorsy, "Ultrafast time-domain spectroscopy based on high-speed asynchronous optical sampling," *Rev. Sci. Instrum.* **78**(3), 035107 (2007).
12. T. Nagatsuma, G. Ducournau, and C. C. Renaud, "Advances in terahertz communications accelerated by photonics," *Nat. Photonics* **10**(6), 371–379 (2016).
13. A. J. Seeds, H. Shams, M. J. Fice, and C. C. Renaud, "TeraHertz photonics for wireless communications," *J. Lightwave Technol.* **33**(3), 579–587 (2015).
14. I. Dan, P. Szriftgiser, E. Peytavit, J. F. Lampin, M. Zegaoui, M. Zaknoute, G. Ducournau, and I. Kallfass, "300 GHz Wireless Link Employing a Photonic Transmitter and Active Electronic Receiver with a Transmission Bandwidth of 54 GHz," *IEEE Trans. THz Sci. Technol.* **10**(3), 271–281 (2020).



15. T. Harter, S. Ummethala, M. Blaicher, S. Muehlbrandt, S. Wolf, M. Weber, M. M. H. Adib, J. N. Kemal, M. Merboldt, F. Boes, S. Nellen, A. Tessmann, M. Walther, B. Globisch, T. Zwick, W. Freude, S. Randel, and C. Koos, "Wireless THz link with optoelectronic transmitter and receiver," *Optica* **6**(8), 1063 (2019).
16. G. Ducournau, P. Szriftgiser, F. Pavanello, E. Peytavit, M. Zaknoute, D. Bacquet, A. Beck, T. Akalin, J. F. Lampin, and J. F. Lampin, "THz communications using photonics and electronic devices: the race to data-rate," *J. Infrared, Millimeter, Terahertz Waves* **36**(2), 198–220 (2015).
17. C. Castro, S. Nellen, R. Elschner, I. Sackey, R. Emmerich, T. Merkle, B. Globisch, D. De Felipe, and C. Schubert, "32 Gbd 16QAM Wireless Transmission in the 300 GHz Band using a PIN Diode for THz Upconversion," in *Optical Fiber Communications Conference and Exhibition (OFC)* (2019), M4F.5.
18. S. Jia, L. Zhang, S. Wang, W. Li, M. Qiao, Z. Lu, N. Idrees, X. Pang, H. Hu, X. Zhang, L. K. Oxenloewe, and X. Yu, "2×300 Gbit/s Line Rate PS-64QAM-OFDM THz Photonic-Wireless Transmission," *J. Light. Technol.* **38**(17), 4715–4721 (2020).
19. D. Damyantov, B. Friederich, M. Yahyapour, N. Vieweg, A. Deninger, K. Kolpatzeck, X. Liu, A. Czyliwlik, T. Schultze, I. Willms, and J. C. Balzer, "High resolution lensless terahertz imaging and ranging," *IEEE Access* **7**, 147704–147712 (2019).
20. L. Valzania, Y. Zhao, L. Rong, D. Wang, M. Georges, E. Hack, and P. Zolliker, "THz coherent lensless imaging," *Appl. Opt.* **58**(34), G256 (2019).
21. S. Nellen, B. Globisch, R. B. Kohlhaas, L. Liebermeister, and M. Schell, "Recent progress of continuous-wave terahertz systems for spectroscopy, non-destructive testing, and telecommunication," *Proc. SPIE* **10531**, 105310C (2018).
22. R. Müller, W. Bohmeyer, M. Kehrt, K. Lange, C. Monte, and A. Steiger, "Novel detectors for traceable THz power measurements," *J. Infrared, Millimeter, Terahertz Waves* **35**(8), 659–670 (2014).
23. S. Nellen, T. Ishibashi, A. Deninger, R. B. Kohlhaas, L. Liebermeister, M. Schell, and B. Globisch, "Experimental Comparison of UTC- and PIN-Photodiodes for Continuous-Wave Terahertz Generation," *J. Infrared, Millimeter, Terahertz Waves* **41**(4), 343–354 (2020).
24. D. Stanze, T. Göbel, R. J. B. Dietz, B. Sartorius, and M. Schell, "High-speed coherent CW terahertz spectrometer," *Electron. Lett.* **47**(23), 1292 (2011).
25. J. Van Rudd and D. M. Mittleman, "Influence of substrate-lens design in terahertz time-domain spectroscopy," *J. Opt. Soc. Am. B* **19**(2), 319–329 (2002).
26. J. Smith, M. Naftaly, S. Nellen, and B. Globisch, "Beam Profile Characterisation of an Optoelectronic Silicon Lens-Integrated PIN-PD Emitter between 100 GHz and 1 THz," *Appl. Sci.* **11**(2), 465 (2021).
27. T. H. Büttgenbach, "An Improved Solution for Integrated Array Optics in Quasi-Optical mm and Submm Receivers: The Hybrid Antenna," *IEEE Trans. Microwave Theory Tech.* **41**(10), 1750–1760 (1993).
28. D. F. Filipovic, S. S. Gearhart, and G. M. Rebeiz, "Double-Slot Antennas on Extended Hemispherical and Elliptical Silicon Dielectric Lenses," *IEEE Trans. Microwave Theory Tech.* **41**(10), 1738–1749 (1993).
29. S. Y. Chen and P. Hsu, "A simplified method to calculate far-field patterns of extended hemispherical dielectric lens," in *Asia-Pacific Microwave Conference Proceedings, APMC (2007)*, (1), pp. 4–7.
30. J. R. Bray and L. Roy, "Performance trade-offs of substrate lens antennas," in *Symposium on Antenna Technology and Applied Electromagnetics, ANTEM 1998* (IEEE, 1998), pp. 321–324.